Journal of the Optical Society of America B
OPTICAL PHYSICS

Synchronization properties of two mutually delay-coupled semiconductor lasers

LEANDRO JUNGES,[1,2] ATHANASIOS GAVRIELIDES,[3] AND JASON A. C. GALLAS[1,2,4,5,*]

[1]Departamento de Física, Universidade Federal da Paraíba, 58051-970 João Pessoa, Brazil
[2]Instituto de Altos Estudos da Paraíba, Rua Infante Dom Henrique 100-1801, 58039-150 João Pessoa, Brazil
[3]Center for High Technology Materials, University of New Mexico, Albuquerque, New Mexico 87106, USA
[4]Institute for Multiscale Simulations, Friedrich-Alexander Universität Erlangen-Nürnberg, D-91052 Erlangen, Germany
[5]Max Planck Institute for the Physics of Complex Systems, Nöthnitzer Str. 38, D-01187 Dresden, Germany
*Corresponding author: jason.gallas@cbi.uni-erlangen.de

Received 12 February 2016; revised 28 March 2016; accepted 29 March 2016; posted 30 March 2016 (Doc. ID 259373); published 27 April 2016

This paper reports a detailed numerical study of the synchronization properties of two mutually delay-coupled semiconductor lasers in the framework of the Lang–Kobayashi model. By computing high-definition stability diagrams, we predict the complex distribution of periodic and chaotic laser oscillations on the coupling versus detuning control parameter plane. Such diagrams provide details concerning the behavior of the laser intensities, quantify objectively the synchronization between their electric fields, and display in-phase and out-of-phase laser behavior. In addition, we also describe the presence of a conspicuous abrupt change in the optimal shift for the greatest value of the cross-correlation function when varying the detuning between the optical angular frequencies of the lasers.

OCIS codes: (140.5960) Semiconductor lasers; (190.0190) Nonlinear optics; (190.3100) Instabilities and chaos.

http://dx.doi.org/10.1364/JOSAB.33.000C65

1. INTRODUCTION

The complex photonics associated with coupled semiconductor lasers offers several possibilities of technological applications and rich dynamical behaviors, as shown by a number of experimental and theoretical studies of phenomena such as chaos synchronization, quasiperiodicity, spontaneous symmetry-breaking of symmetric laser configurations, bubbling, etc. [1–10].

Synchronization properties between mutually delay-coupled lasers have also been extensively analyzed. For weak coupling, Hohl *et al.* [11] have shown that two nonidentical mutually delay-coupled semiconductor lasers can present localized synchronization where the amplitude of one of the lasers is significantly greater than the other. Symmetry breaking of periodic solutions at a low coupling rate in perfectly symmetric mutually delay-coupled lasers was reported by Rogister and Garcia-Ojalvo [12]. Interesting theoretical and experimental studies of subnanosecond coupling-induced synchronized chaotic dynamics in conjunction with spontaneous symmetry-breaking in the system have been done by Heil *et al.* [13]. Chaotic achronal synchronization for two distant mutually coupled semiconductor lasers was observed experimentally and theoretically by Mulet *et al.* [14]. The potentialities and intricacies of delay coupled lasers are discussed in a recent and encompassing survey by Soriano *et al.* [2]. Despite all these works, little is currently known about the impact of the simultaneous variation of multiple control parameters of the lasers on their synchronization properties.

A recent study [15] of the control parameters of two mutually delay-coupled semiconductor lasers has shown the disappearance of an abundant type of periodic oscillation called regular pulse packages (RPPs) [16], characterized by a sequence of packages composed of decreasing amplitude pulses, when the angular frequencies of the lasers contain a very small frequency detuning $\delta \equiv \omega_2 - \omega_1$, of the order of 100 times smaller than the relaxation frequency of the lasers oscillations. However, when the detuning δ between the lasers is continuously varied over large ranges, RPPs can periodically recur in specific windows of δ in control space [15].

In this work, we provide additional information concerning details of the aforementioned recurrence of RPP windows. More specifically, we describe how the periodic and chaotic phases emerge and provide an in-depth analysis of the synchronization properties of the laser modes involved. To this end, we introduce an *indicator* that quantifies the synchronization between the lasers. This indicator is numerically computed for wide ranges of the frequency detuning and coupling coefficient between the lasers. In addition, we also calculate the well-known cross-correlation function between the lasers' intensities, analyzing its maximum value and optimal shift in order

to quantify laser performance when laser detuning is varied over large ranges. Similar procedures have been extensively used in technological applications such as, for example, optical coherence tomography [17], synchronization of vehicle sensors [18], and underwater sonar imaging [19].

2. MODEL

The two mutually delay-coupled semiconductor lasers studied here are governed by the equations [15,20]

$$\dot{E}_1 = (1 + i\alpha)N_1E_1 + \eta e^{-i\omega\tau}E_2(t - \tau), \quad (1)$$

$$T\dot{N}_1 = P - N_1 - (1 + 2N_1)|E_1|^2, \quad (2)$$

$$\dot{E}_2 = (1 + i\alpha)N_2E_2 + \eta e^{-i\omega\tau}E_1(t - \tau) + i\delta E_2, \quad (3)$$

$$T\dot{N}_2 = P - N_2 - (1 + 2N_2)|E_2|^2. \quad (4)$$

Here, $E_{1,2}(t)$ are the normalized slowly varying complex electric fields while $N_{1,2}(t)$ are the normalized excess carrier numbers for lasers 1 and 2, respectively. In these equations, the optical angular frequency of laser 1 is used as reference, so that $\omega = \omega_1$, while the detuning frequency is $\delta \equiv \omega_2 - \omega_1$. Time is normalized to the cavity photon lifetime (~1 ps), and T is the ratio of the carrier lifetime (~1 ns) to the photon lifetime. The delay time τ represents the flying time of the light between the lasers, η controls the strength of the symmetric coupling, δ controls the magnitude of the detuning between the lasers, P is the normalized pump current above threshold, and α is the linewidth enhancement factor. Parameters are fixed at realistic values [15,16,20]: $T = 1710$, $\alpha = 5$, $P = 1.155$, $\tau = 10$, $\eta = 0.255$, $\omega = -0.01962$. As for initial configurations, we use $N_{1,2}(0) = 1$ and $E^r_{1,2}(t') = E^i_{1,2}(t') = 1$ for $-\tau \le t' \le 0$, where $E_{1,2}(t) = E^r_{1,2}(t) + iE^i_{1,2}(t)$. The numerical results presented below were obtained by solving Eqs. (1)–(4) using the standard fourth-order Runge-Kutta algorithm, with a fixed time step $h = 0.005$. *Ad hoc* tests indicate that, for realistic physical parameters, the final results are not sensitive to these assumptions. For additional details concerning the computation of stability diagrams, see Section 2 of the survey in [21].

3. RESULTS

The behavior of the lasers' outputs can be classified as a function of the parameters using the so-called *isospike diagrams* [15,22,23]. As exemplified by Figs. 1(a) and 1(c), isospike diagrams classify the laser output using 14 colors to represent periodic oscillations, according to their number of peaks (local maxima) per period. Oscillations having more than 14 peaks per period are represented by "recycling colors modulo 14," i.e., the color index used is obtained as the remainder of the integer division of the number of peaks by 14. Solutions with 15 peaks per period are marked with the same color associated with one peak, 16 spikes are marked with same color of two peaks, and so on. Multiples of 14 were given the index 14.

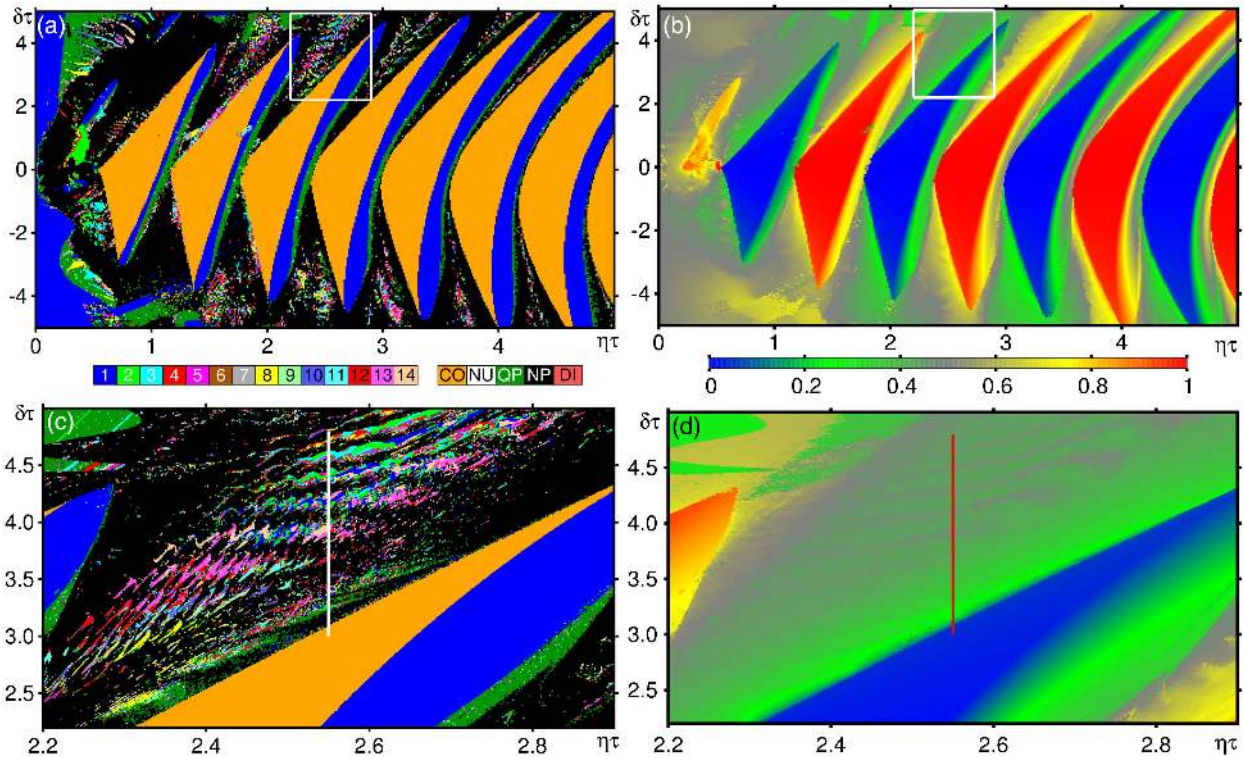

Fig. 1. Left and right columns contrast two complementary ways of recording periodic and aperiodic phases in parameter space. (a) Isospike diagram, recording the number of spikes per period of periodic modes. (b) Diagram displaying the synchronization ratio r as a function of the coupling η and the detuning δ, scaled by the constant delay time $\tau = 10$. Panels (c) and (d) are magnifications of the white boxes in (a) and (b), respectively. The vertical lines are discussed in Fig. 2. In an accompanying video, we present an animation of similar panels over a wide range of τ values (Visualization 1).

In this way, all periodic pulses can be accommodated with a palette of 14 colors. In addition, non-zero fixed points, representing constant output, are plotted in orange, quasiperiodic solutions are plotted in dark green, lack of numerically detectable periodicity is plotted in black, null output is plotted in white, and divergent solutions are plotted in light red. These specific solutions are indicated on the bar located below Fig. 1(a) and next to the isospike color bar. The diagrams presented in Fig. 1 take laser 1 into account, but laser 2 presents the same qualitative behavior.

Figure 1(a) illustrates laser behavior as a function of the coupling strength η and the detuning δ, both scaled by the constant delay time τ. The main dynamical properties of this system depend on the emergence of the so-called compound laser modes (CLMs) [15], which represent CW solutions and depend on the scaled parameters $\eta\tau$ and $\delta\tau$. The consideration of scaled parameters avoids an undesired "zoom out" effect (see [15]) and facilitates comparison between diagrams when the delay is increased. Figure 1(a) presents a sequence of triangular shaped islands of constant output, placed over a background of aperiodic solutions (in black). Such islands repeat horizontally, along the direction of increasing coupling and no detuning ($\delta = 0$). On the right-hand side of the triangular islands, we find transitions from CW output (in orange), to one-peak oscillations (blue), to quasiperiodic oscillations (dark green), finally reaching the domain of aperiodic oscillations (black).

Figure 1(a) shows a $\eta\tau \times \delta\tau$ diagram for a fixed value of the delay ($\tau = 10$). In the supplementary material (see Visualization 1), we show a video detailing how the variation of the delay over the interval (0, 30) influences the control plane. Initially, for relatively small delays, one sees a big red phase of divergent solutions, which disappear toward the right side of the diagram as τ is increased. For small delays, the phases of divergent solutions are associated with strong coupling between the lasers. Note that the axes in the diagrams are scaled by the delay time, given in each frame of the film. Thus, as we wanted to keep the product $\eta\tau$ constant for clarity reasons, smaller delays require bigger couplings. The range of coupling values covered in the video is so wide that it may contain some small regions where the laser intensity diverges to infinity. Of course, this happens because either the rate equation assumptions are violated or, for a fixed step size, the accuracy in the numerical calculations degrades and produces divergent solutions. In this paper, we have not investigated this perhaps very interesting result and did not focus on whether stable and convergent solutions were possible if the accuracy of the calculation was increased. Such an investigation would require a previous experimental validation of the model and a considerable additional investment of computer resources. As the delay increases, η becomes small and the divergence region is displaced to increasingly larger values of $\eta\tau$. Also, a "burst" of periodic solutions is observed over the aperiodic black phase, between the triangular CW phases. The size of these periodic phases is maximum for $\tau \sim 8.5$. In addition, the triangular phases seem to shrink continuously as the delay increases more and more.

As already mentioned, previous work has shown that the transition from 0 to very small values of the detuning δ makes the RPPs disappear [15]. However, over a specific region of the parameter space, such solutions may reappear for $\delta \neq 0$, in a way that a steady increase of the detuning in this region reveals an alternation between RPPs and aperiodic solutions [15]. Here, the region inside the white box in Fig. 1(a), magnified in Fig. 1(c), presents such alternation between phases in a more general and elucidative way. It can be shown that the colored stripes in Fig. 1(c), representing solutions with more than one peak per period, are basically related to RPPs phases [examples of solutions over these phases are shown in Figs. 2(c) and 2(e)]. The complex structure and disposition of the stripes related to RPPs presented in this diagram evidence that the fairly regular alternation between RPPs and aperiodic phases results from the analysis of the variation of a single parameter, which follows a specific path through the diagram [15]. The 2D approach presented here greatly complements this earlier analysis, providing a deeper insight concerning the intricate relation between laser phases.

For a better understanding of the synchronization properties of lasers, we calculated a synchronization parameter, defined by the ratio

$$r = \frac{\langle |E_1(t) + E_2(t)|^2 \rangle}{2(\langle |E_1(t)|^2 \rangle + \langle |E_2(t)|^2 \rangle)}, \tag{5}$$

where $\langle \cdot \rangle$ denotes time average. In-phase laser fields are characterized by $r = 1$, while out-of-phase fields imply $r = 0$. Figure 1(b) displays the synchronization parameter r for the same window of $\eta\tau$ and $\delta\tau$ in Fig. 1(a). From the figure, one sees that "islands" of CW output display an alternation of in-phase (red) and out-of-phase (blue) oscillations of the laser fields. Such in- and out-of-phase oscillations were studied before (see, for example, [24] and [25]). Here, our aim is to describe their relative abundance and organization in the laser control space. The regions dominated by aperiodic phases have $r \sim 0.5$ (gray). The region of RPPs, indicated by the white box, is magnified in Fig. 1(d). It shows a clear alternation of gray stripes (aperiodic solutions) and green stripes, related to the RPPs phases. The fact that the RPPs phases present a value of r smaller than the ones of the aperiodic phases suggest that, for virtually all RPPs in that windows, the laser fields are slightly out of phase.

Figure 2 presents details of the lasers outputs on the stripes presented in Figs. 1(c) and 1(d). Figure 2(a) shows a bifurcation diagram calculated along the vertical white line in Fig. 1(c). The local maxima of the lasers' intensities are presented in green for laser 1 and in red for laser 2. Despite the fact that both lasers are identical (have the same pump current and coupling coefficient), the difference in the optical angular frequencies induces a larger average pulse amplitude for laser 2 over the entire range of δ. An analogous bifurcation diagram (not shown here) shows that a larger amplitude of laser 1 is observed when changing δ by $-\delta$.

As seen in Fig. 1(c), the vertical white line crosses the stripes alternating aperiodic solutions (black) and RPPs (several colors). This alternation is observed in the diagram of Fig. 2(a) as recurrent windows of periodic solutions interspersed with windows of aperiodic oscillations. The vertical blue lines (c)–(f) indicate some of this interspersed windows.

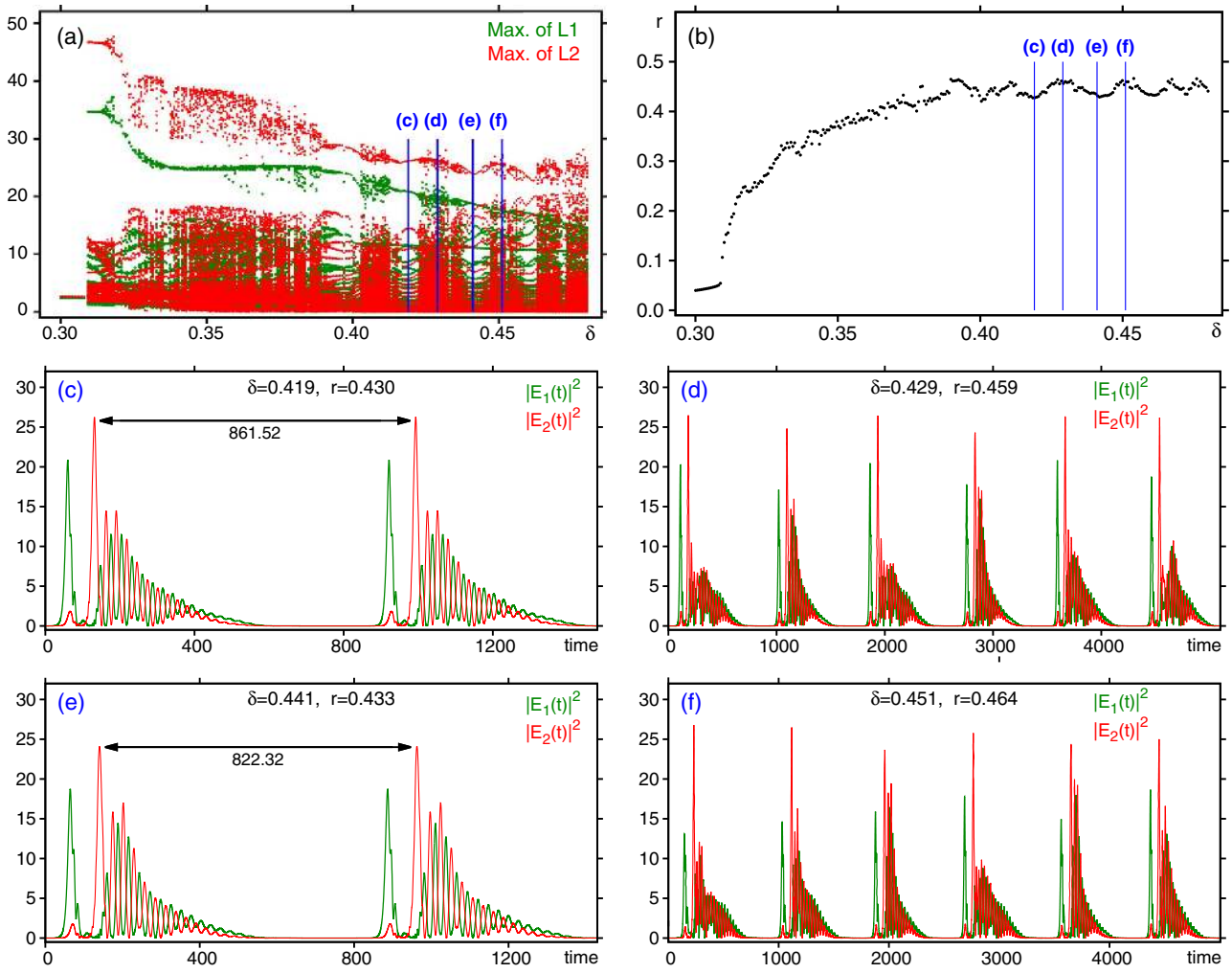

Fig. 2. Details of the laser outputs on the stripes presented in Fig. 1. (a) Bifurcation diagram as a function of the detuning δ. (b) Synchronization parameter r, both calculated along the vertical lines seen in Figs. 1(c) and 1(d), respectively ($\eta = 0.255$). Panels (c)–(f) show temporal evolutions of the laser intensities for selected values of δ, green for laser 1 and red for laser 2, revealing an alternation between RPPs, in (c) and (e), and aperiodic solutions, in (d) and (f).

Figure 2(b) shows the synchronization parameter r calculated for the same values of δ as in Fig. 1(a). They were obtained along the vertical red line in Fig. 1(d). An increase in δ along that line leads to an increase in the synchronization parameter from $r \sim 0.05$, when the lasers' intensities were constant, until $r \sim 0.45$, where the intercalation between RPPs and aperiodic outputs takes place. In this last region, r presents small oscillations, small values of r being associated with RPPs, and larger values with aperiodic oscillations. This feature is evident in the temporal evolution of the lasers' intensities calculated for detunings arbitrarily chosen in this window.

The temporal evolutions presented in Figs. 2(c)–2(f) are calculated for δ values corresponding to the labeled vertical lines in the diagrams of Figs. 2(a) and 2(b). For $\delta = 0.419$, Fig. 2(c) shows the temporal evolution for the laser 1 intensity, in green, and in red for laser 2. Both intensity profiles are quite similar, but the periodic sequence of amplitude decaying pulses, characterizing RPPs, are slightly out of phase. In this case, the synchronization parameter is $r = 0.430$. When the detuning is increased to $\delta = 0.429$, Fig. 2(d) shows that the solution is no longer periodic. Although the intensity profiles remain similar to the RPPs observed above for $\delta = 0.419$, now the pulse packages do not repeat in time. Such solutions, with profiles very similar to RPPs but aperiodic, may be called irregular pulse packages [26] or "quasi-RPPs" [15,27]. For this aperiodic solution, we find $r = 0.459$, slightly greater than what is obtained for the previous RPPs. By continuously increasing the detuning, a sequential alternation of the two solutions above is observed, as illustrated in Figs. 2(e) and 2(f). The synchronization parameter values for RPPs are $r \sim 0.43$, while for quasi-RPPs they are slightly greater, namely $r \sim 0.46$.

The above analysis was complemented by evaluating the cross-correlation function for solutions presented on the diagrams of Figs. 2(a) and 2(b). The cross-correlation function is defined as [1,3]

$$C(\Theta) = \frac{\langle [I_1(t) - \langle I_1(t)\rangle][I_2(t+\Theta) - \langle I_2(t)\rangle]\rangle}{\sqrt{\langle [I_1(t) - \langle I_1(t)\rangle]^2\rangle \langle [I_2(t) - \langle I_2(t)\rangle]^2\rangle}}, \quad (6)$$

where $I_j(t) = |E_j(t)|^2$ and Θ is the temporal shift in $I_2(t)$. For each solution of Eqs. (1)–(4), we can calculate $C(\Theta)$ and verify what is the optimal temporal shift (Θ_M) to maximize the correlation between the lasers.

The top panel in Fig. 3 shows the maximum cross-correlation function $C(\Theta_M)$, multiplied by 100 for graphical clarity, and the optimal temporal shift (Θ_M) for solutions calculated for δ along the vertical lines in Figs. 1(c) and 1(d). This is an extremely laborious numerical task, given that, for each value of δ, it is necessary to calculate $C(\Theta)$ for several temporal shifts Θ in order to determine which shift maximizes the correlation. The diagram presented in Fig. 3 (top) was calculated for 400 values of δ and, for each one of these values, an additional 40,000 temporal shifts in the interval $-100 \le \Theta \le 100$ were investigated. The generation of this diagram required 11.4 h of numerical calculation, using 50 fast processors of a SGI Altix cluster, each one operating at a nominal clock speed of 2.9 GHz.

Figure 3 shows (black, top row) the maximum cross correlation between the lasers' intensities. The cross correlation

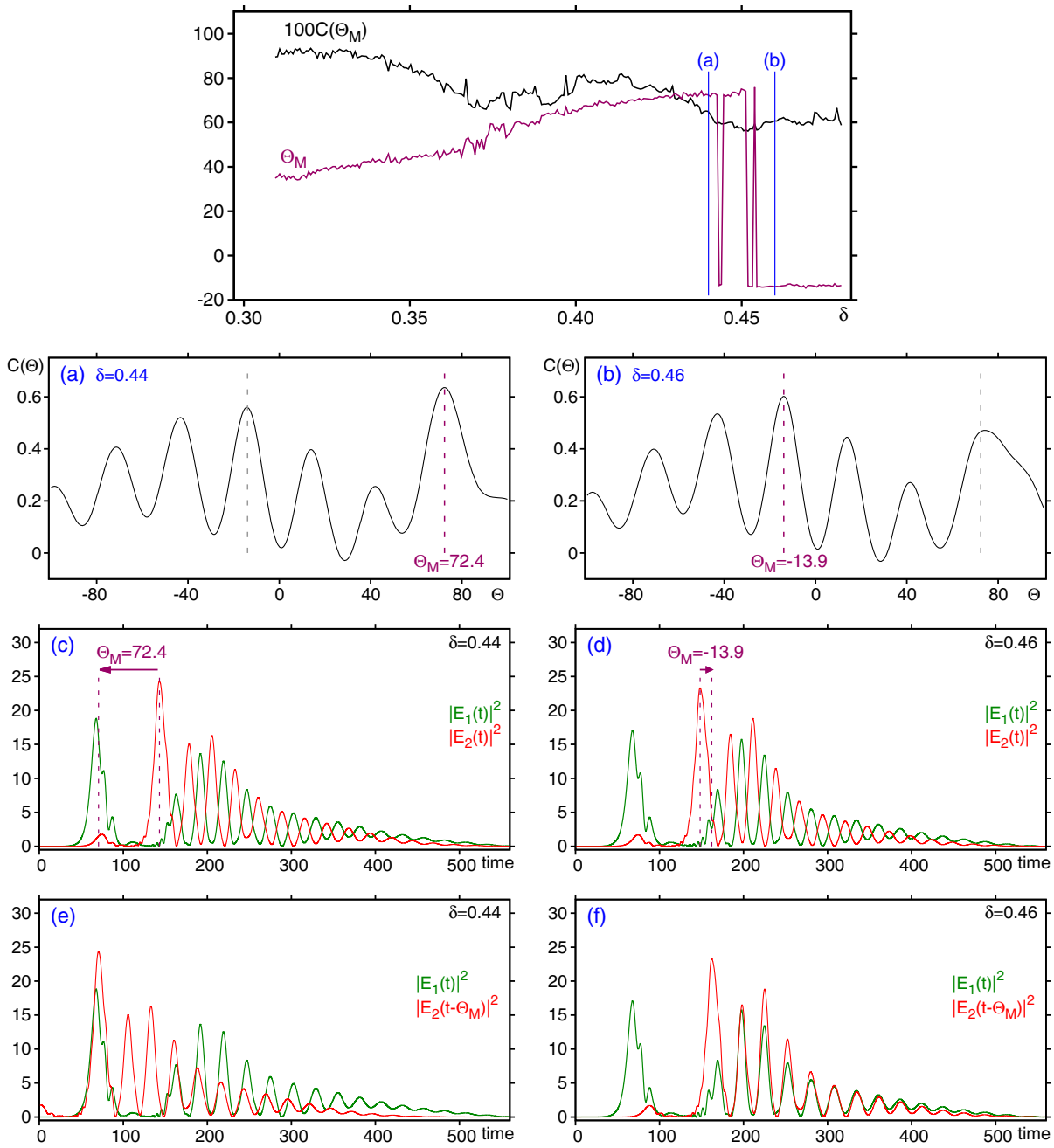

Fig. 3. (Top) Maximum cross-correlation function $C(\Theta_M)$, multiplied by 100 for graphical reasons, and optimal temporal shift Θ_M, calculated as a function of the detuning. (a) and (b) Cross-correlation function calculated for detuning before and after the abrupt drop in Θ_M, evidencing the change in the position of the global maximum. (c) and (d) Temporal evolution of the intensities of lasers 1 and 2, for detuning before and after the drop, indicating the optimal temporal shift. (e) and (f) Same temporal evolutions as (c) and (d), but with the optimal shifts performed.

cannot be defined for CW outputs (in the initial range $0.300 < \delta < 0.309$) because for these solutions $I_{1,2}(t) = \langle I_{1,2}(t) \rangle$ [see Eq. (6)]. As the detuning is increased above $\delta = 0.309$, $C(\Theta_M)$ decreases continuously but always stays $\gtrapprox 0.6$. The maximum correlation does not drop too much because the profiles of the RPPs (or "quasi-RPPs") related to the intensities of both lasers are similar to each other, making it possible to match them in a fairly good way.

The top panel of Fig. 3 also shows the optimal time shift related to the maximum cross-correlation between the intensities. For $0.309 < \delta < 0.450$, Θ_M grows almost linearly from $\Theta_M \sim 35$ until $\Theta_M \sim 75$. Near $\delta = 0.45$, the optimal shift sharply drops to $\Theta_M \sim -13.5$, remaining so for additional detunings. This sudden drop of the optimal shift can be understood analyzing the cross-correlation function for solutions immediately before and after the drop. Figure 3(a) shows the cross-correlation function for $\delta = 0.44$, immediately before the drop. The maximum correlation is $C(\Theta_M) = 0.636$, obtained for a shift $\Theta_M = 72.4$. This maximum is indicated by the purple dashed line (the rightmost dashed line). At this point, it is important to notice that the second largest value of $C(\Theta)$ is obtained for $\Theta = -14.2$, as indicated by the leftmost vertical gray dashed line.

Figure 3(b) shows that, by increasing the detuning to $\delta = 0.46$, the profile of the cross-correlation function is deformed in a way that the amplitude of the maximum of $C(\Theta)$ located near $\Theta \sim -14$ becomes bigger than the one near $\Theta \sim 72$. In this case, the optimal shift is $\Theta_M = -13.9$, indicated in Fig. 3(b) by the purple dashed line (left). The gray dashed line (right) indicates the position of the optimal shift before the drop ($\Theta = 72.4$). To summarize, the continuous deformation on the intensity profiles of both lasers, driven by the gradual increase of δ, is manifested by a continuous deformation of the cross-correlation function. This function deforms in a way that, for $\delta \sim 0.45$, the local maximum at $\Theta \sim -14$ surpasses the amplitude of the so far global maximum, located in $\Theta \sim 72$. This crossover is responsible for the abrupt drop observed for Θ_M in Fig. 3 (top).

Figures 3(c) and 3(d) show the temporal evolution of the lasers intensities, before and after the drop, respectively. Purple arrows indicate the shift in $|E_2(t)|$, which corresponds to the configuration of maximum cross correlation between the intensities. Right below it, in Figs. 3(e) and 3(f), the intensities are plotted with the optimal shift applied in the intensity of laser 2, manifesting explicitly the optimal configuration for the correlation.

4. CONCLUSIONS

This paper investigated synchronization properties between two mutually delay-coupled lasers as a function of the detuning between the optical angular frequencies of the lasers. The distribution of periodic and chaotic phases was mapped in detail on the control parameter plane defined by the coupling coefficient and the detuning ($\eta\tau \times \delta\tau$). Such a plane was found to display a sequential appearance of self-similar stability islands of CW output, along the $\delta\tau = 0$ axis. By considering a synchronization indicator r, we found that the alternation of stability islands is related to an alternation between in-phase and out-of-phase oscillations of the lasers fields [25]. In addition, we showed the recurrent appearance of RPPs near these islands, interspersed with windows of aperiodic "quasi-RPPs" solutions. The synchronization parameter r was found to be slightly smaller inside RPPs windows, suggesting an out-of-phase disposition of the laser electric fields. A remarkably abrupt change in the optimal temporal shift, which maximizes the cross-correlation function between the laser intensities, was found for $\delta \sim 0.45$. Such a jump was shown to be related to continuous deformations of the temporal profile of I_1 and I_2 induced by a continuous increment of δ. We hope our findings motivate their experimental investigation.

Funding. Conselho Nacional de Desenvolvimento Científico e Tecnológico (CNPq) (150898/2014-2); Deutsche Forschungsgemeinschaft (DFG); Max Planck Institute for the Physics of Complex Systems.

Acknowledgment. L. J. was supported by a CNPq postdoctoral fellowship, project 150898/2014-2. J. A. C. G. was supported by CNPq/Brazil. All bitmaps were computed on the CESUP- UFRGS clusters, located in Porto Alegre, Brazil. This work was also supported by the Deutsche Forschungsgemeinschaft through the Cluster of Excellence Engineering of Advanced Materials and by the Max Planck Institute for the Physics of Complex Systems, Dresden, in the framework of the Advanced Study Group on Optical Rare Events.

REFERENCES

1. A. Quirce, A. Valle, H. Thienpont, and K. Panajotov, "Chaos synchronization in mutually coupled 1550-nm vertical-cavity surface-emitting lasers with parallel polarizations and long delay time," J. Opt. Soc. Am. B **33**, 90–98 (2016).
2. M. C. Soriano, J. Garcia-Ojalvo, C. R. Mirasso, and I. Fischer, "Complex photonics: dynamics and applications of delay-coupled semiconductors lasers," Rev. Mod. Phys. **85**, 421–470 (2013).
3. D. A. Arroyo-Almanza, A. N. Pisarchik, I. Fischer, C. R. Mirasso, and M. C. Soriano, "Spectral properties and synchronization scenarios of two mutually delay-coupled semiconductor lasers," Opt. Commun. **301**–302, 67–73 (2013).
4. N. Oliver, T. Jüngling, and I. Fischer, "Consistency properties of a chaotic semiconductor laser driven by optical feedback," Phys. Rev. Lett. **114**, 123902 (2015).
5. X. J. Yang, J. G. Wu, Y. Li, L. Wang, and G. Q. Xia, "Time-delay signatures hidden in the phase of chaotic output of mutually delay-coupled vertical-cavity surface-emitting lasers," Opt. Commun. **336**, 262–268 (2015).
6. I. Fischer, Y. Liu, and P. Davis, "Synchronization of chaotic semiconductor laser dynamics on subnanosecond time scales and its potential for chaos communication," Phys. Rev. A **62**, 011801 (2000).
7. I. Ermakov, S. T. Kingni, V. Z. Tronciu, and J. Danckaert, "Chaotic semiconductor ring lasers subject to optical feedback: applications to chaos-based communications," Opt. Commun. **286**, 265–272 (2013).
8. A. Hohl, A. Gavrielides, T. Erneux, and V. Kovanis, "Quasiperiodic synchronization for two delay-coupled semiconductor lasers," Phys. Rev. A **59**, 3941–3949 (1999).
9. V. Flunkert, O. D'Huys, J. Danckaert, I. Fischer, and E. Schöll, "Bubbling in delay-coupled lasers," Phys. Rev. E **79**, 065201 (2009).
10. H. Liu, B. Ren, Q. Zhao, and N. Li, "Characterizing the optical chaos in a special type of small networks of semiconductor lasers using permutation entropy," Opt. Commun. **359**, 79–84 (2016).

11. A. Hohl, A. Gavrielides, T. Erneux, and V. Kovanis, "Localized synchronization in two coupled nonidentical semiconductor lasers," Phys. Rev. Lett. **78**, 4745–4748 (1997).
12. F. Rogister and J. Garcia-Ojalvo, "Symmetry breaking and high-frequency periodic oscillations in mutually coupled laser diodes," Opt. Lett. **28**, 1176–1178 (2003).
13. T. Heil, I. Fischer, W. Elsasser, J. Mulet, and C. Mirasso, "Chaos synchronization and spontaneous symmetry-breaking in symmetrically delay-coupled semiconductor lasers," Phys. Rev. Lett. **86**, 795–798 (2001).
14. J. Mulet, C. Mirasso, T. Heil, and I. Fischer, "Synchronization scenario of two distant mutually coupled semiconductor lasers," J. Opt. B **6**, 97–105 (2004).
15. L. Junges and J. A. C. Gallas, "Stability diagrams for continuous wide-range control of two mutually delay-coupled semiconductor lasers," New J. Phys. **17**, 053038 (2015).
16. T. Heil, I. Fischer, W. Elsäßer, and A. Gavrielides, "Dynamics of semiconductor lasers subject to delayed optical feedback: the short cavity regime," Phys. Rev. Lett. **87**, 243901 (2001).
17. Y. Li, G. Gregory, B. L. Lam, and P. J. Rosenfeld, "Automatic montage of SD-OCT data sets," Opt. Express **19**, 26239–26248 (2011).
18. L. Fridman, D. E. Brown, W. Angell, I. Abdic, B. Reimer, and H. Y. Noh, "Automated synchronization of driving data using vibration and steering events," arXiv:1510.06113 (2015).
19. N. Kumar, A. C. Lammert, B. Englot, F. S. Hover, and S. S. Narayanan, "Directional descriptors using Zernike moment phases for object orientation estimation in underwater sonar images," in *IEEE International Conference on Acoustics Speech and Signal Processing (ICASSP)*, (2011), pp. 1025–1028.
20. F. Rogister and M. Blondel, "Dynamics of two mutually delay-coupled semiconductor lasers," Opt. Commun. **239**, 173–180 (2004).
21. J. A. C. Gallas, "Systematics of spiking in some CO_2 laser models," Adv. Atom. Mol. Opt. Phys. **65**, in print (2016).
22. J. G. Freire and J. A. C. Gallas, "Stern-Brocot trees in the periodicity of mixed-mode oscillations," Phys. Chem. Chem. Phys. **13**, 12191–12198 (2011).
23. M. R. Gallas, M. R. Gallas, and J. A. C. Gallas, "Distribution of chaos and periodic spikes in a three-cell population model of cancer," Eur. Phys. J. Spec. Top. **223**, 2131–2144 (2014).
24. J. Javaloyes, P. Mandel, and D. Pieroux, "Dynamical properties of lasers coupled face to face," Phys. Rev. E **67**, 036201 (2003).
25. H. Erzgräber, B. Krauskopf, and D. Lenstra, "Compound laser modes of mutually delay-coupled lasers," SIAM J. Appl. Dyn. Syst. **5**, 30–65 (2006).
26. T. Heil, I. Fischer, W. Elsäßer, B. Krauskopff, K. Green, and A. Gavrielides, "Delay dynamics of semiconductor lasers with short external cavities: bifurcation scenarios and mechanisms," Phys. Rev. E **67**, 066214 (2003).
27. L. Junges, T. Pöschel, and J. A. C. Gallas, "Characterization of the stability of semiconductor lasers with delayed feedback according to the Lang-Kobayashi model," Eur. Phys. J. D **67**, 149 (2013).